Cost-Function-Based Microgrid Decentralized Control of Unbalance and Harmonics for Simultaneous Bus Voltage Compensation and Current Sharing

Jia Liu, *Member, IEEE*, Yushi Miura, *Member, IEEE*, and Toshifumi Ise, *Member, IEEE*

***Abstract*—Power quality of inverter-based microgrids is a challenging issue due to nonlinearities of inverters, multiple resonance modes of network impedance, and unbalanced and nonlinear loading condition. The ideal solution is to assure the best power quality at the common bus to which loads are connected, and share the negative and harmonic sequence currents between the inverters without any communication. However, it is difficult to achieve this objective with existing virtual-impedance-based methods when nonlinearities of inverters, e.g., dead time, are not negligible. In this paper, a novel cost-function-based method is proposed to solve this problem. The proposed cost functions are optimized using continuous-control-set model predictive control. As unknown nonlinearities of inverters can be observed by introducing disturbance models, even when they are not negligible, the presented method can compensate bus voltage unbalance and harmonics and share the compensated current between inverters autonomously, with neither communication nor upper level controller. Parameter tuning of the proposed method is the key to achieve the balance between bus voltage quality and current sharing, and between stability and fast response. Experimental results demonstrate that the proposed control scheme is effective even under conditions of large inverter nonlinearities.**

***Index Terms*—Cost function, dc–ac power converters, decentralized control, distributed power generation, microgrids, model predictive control (MPC), power conversion harmonics, power quality, pulsewidth modulation (PWM) converters, three-phase unbalance.**

I. Introduction

THE concept of the microgrid has been developed through recent decades to facilitate the integration of distributed generators (DGs), especially inverter-interfaced DGs into the utility [1]. In ac microgrids, inverters and loads are usually connected to one or multiple ac buses, as shown in Fig. 1. The power quality of the bus voltage is very important in these kinds of configurations. If the bus voltage is unbalanced and/or

Manuscript received July 10, 2018; revised September 30, 2018 and October 26, 2018; accepted October 29, 2018. Date of publication November 1, 2018; date of current version May 22, 2019. This paper was presented in part at the 2017 IEEE Energy Conversion Congress and Exposition (ECCE), Cincinnati, OH, USA, in October 2017. Recommended for publication by Associate Editor A. Davoudi. *(Corresponding author: Jia Liu.)*

The authors are with the Division of Electrical, Electronic and Information Engineering, Osaka University, Osaka 565-0871, Japan (e-mail:

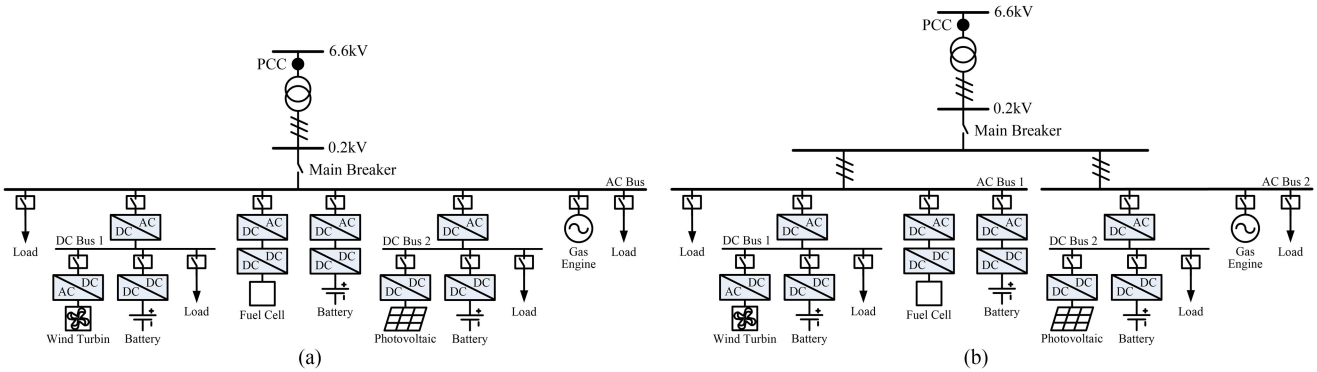

Fig. 1. Examples of (a) single-ac-bus microgrid and (b) multiple-ac-bus microgrid.

out that positive virtual impedances at harmonic sequences can improve the harmonic current sharing, and this method is further developed through [6]–[8]. However, increased output impedances at harmonic sequences lead to a more distorted bus voltage. To address this drawback, methods based on negative virtual impedances to cancel harmonic voltage drops over the line impedance are proposed in [9] and [10]. These methods are effective in simultaneous harmonic current sharing and bus voltage quality improvement, if nonlinearities of the inverter are negligible. However, when nonlinearities of the inverter are not negligible, they will easily cause circulating harmonic currents between inverters and deteriorate the bus voltage quality, because the impedance between inverters and common bus are largely reduced by negative virtual impedances. In fact, in order to alleviate harmonic currents resulted from nonlinear features of inverters, positive virtual impedance should be used [11]. From these previous studies, it can be concluded that the bus voltage quality and mitigation of inverter nonlinearities seem to be an intrinsic tradeoff if the virtual-impedance-based methods are applied. This dilemma is further discussed in Section II of this paper. Direct modification of the inverter impedance rather than reshaping the line impedance is proposed in [12]; however, nonlinearities of inverters are still not considered in this study.

Another communication-less approach is to share the harmonic power in a similar manner to that of the fundamental power, such as a harmonic droop controller proposed in [13]. However, the bus voltage quality is not intentionally controlled in this method. A $G-H$ droop proposed in [14] mixes the concept of the harmonic droop and virtual impedance. The $G-H$ droop is equivalent to a virtual resistance in parallel with the inverter impedance, in order to reduce the overall inverter impedance. However, the resulted reduction of the inverter impedance is quite limited [12] and the intrinsic tradeoff of the virtual-impedance-based method is still a concern.

The performance of the virtual-impedance-based method can be improved with communication and upper level controller [15]–[17]. In [15], bus voltage information is sent to the DGs in order to adjust the virtual impedance added to the DGs. In [16], detection signals from the central controller are required to select the compensation mode, and the virtual impedances are finally adjusted through an intentional real power disturbance injection method. In [17], each DG receives bus voltage information to calculate the respective compensation current for the bus voltage quality restoration. In view of the additional infrastructure and probable communication failure, communication-based methods are always less preferable if their performance can be reached by communication-less methods.

Another method considering simultaneous voltage and current compensation is reported in [18]; however, two inverters are needed for one DG, and the current sharing between multiple DGs is not demonstrated in this paper. Unbalanced and nonlinear voltage compensation using H_∞ control for the load voltage is proposed in [19], and unbalanced voltage compensation using the model predictive control (MPC) for the local voltage is proposed in [20]; however, in both methods, compensation current sharing between inverters is not addressed.

To summarize, existing unbalance and harmonics control methods for simultaneous bus voltage compensation and current sharing are mainly based on negative virtual impedance. However, this principle is not applicable if inverter nonlinearities are not negligible. Therefore, there is no proper design of existing methods to ensure the bus voltage quality and share load current, simultaneously, when inverter nonlinearities are not negligible. In view of this blank, we propose a cost-function-based method in [21] and further develop it in this paper. Optimization of the proposed cost functions are realized by MPC, which is an effective multiple-input–multiple-output control method insensitive to model mismatch and has been adopted in inverter control applications thanks to the progress of the digital signal processor (DSP) embedded in inverters [22]–[27]. The MPC applied in inverters can be classified as finite control set (FCS-MPC) or continuous control set (CCS-MPC) [26]. The former includes the modulation part into the MPC and the latter use MPC to generate the voltage reference for the conventional pulsewidth modulation (PWM). Generally, FCS-MPC generates more harmonics around switching frequency [26], which makes its application in microgrids quite challenging [27]. Besides, computational complexity of the FCS-MPC is higher than that of the CCS-MPC [26]. Therefore, the CCS-MPC is adopted in the proposed control scheme.

With the proposed control scheme in [21], bus voltage compensation and unbalanced and harmonic current sharing between inverters can be achieved simultaneously, with neither

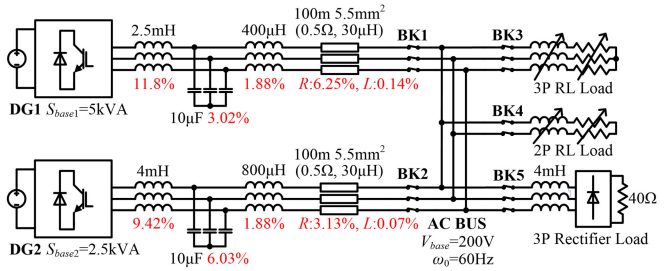

Fig. 2. Circuit of the studied microgrid.

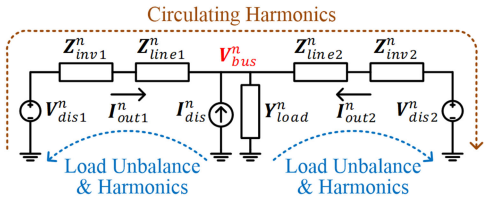

Fig. 3. Principle of virtual-impedance-based methods for nth-order harmonic sequence.

central controller nor communication, and even without direct bus voltage measurement, which is usually not available for inverter-interfaced DGs considering the physical distance between the bus and inverter-interfaced DGs in field application. This method can be easily integrated into any decentralized control scheme of parallel inverters with acceptable computational complexity in the DSP. In this paper, this method is further developed by considering the nonlinear features of inverters in the plant model to simultaneously suppressing circulating harmonic currents caused by inverter nonlinearities and improving the bus voltage quality. As it is mentioned previously, it is difficult to achieve this objective with any reported methods. Moreover, parameter tuning of the MPCs is further developed through pole analyses of complete closed-loop models of the microgrid for better dynamic response, and the analogy between the proposed cost functions and the well-known droop control is illustrated to facilitate understanding of the mechanism of the proposed control. Finally, experimental results are presented in this paper to verify the effectiveness of the proposed method under conditions of large inverter nonlinearities.

II. Limitation of Virtual-Impedance-Based Methods

In this section, the limitation of virtual-impedance-based methods, i.e., intrinsic traded-off between the bus voltage quality and mitigation of inverter nonlinearities is explained.

Fig. 2 shows a typical single-bus microgrid studied in this paper, in which a 5-kVA inverter and a 2.5-kVA inverter are connected to a 200-V/60-Hz bus in parallel through respective *LCL* filter and feeder line. Different types of load are connected to the common bus, and some of them introduce unbalance and/or harmonics. The simplified equivalent circuit of this microgrid at nth-order harmonic sequence can be modeled as Fig. 3, where $\boldsymbol{Z}^n_{\text{line}k}$ and $\boldsymbol{Z}^n_{\text{inv}k}$ represent the line impedance and inverter impedance of kth inverter, respectively, $\boldsymbol{I}^n_{\text{out}k}$ and $\boldsymbol{V}^n_{\text{bus}}$ represents the output current of kth inverter and bus voltage, respectively, and $\boldsymbol{I}^n_{\text{dis}}$ and $\boldsymbol{Y}^n_{\text{load}}$ represent the Norton's equivalent circuit of the load. In this paper, the superscript n indicates the nth-order sequence.

Similar equivalent circuit can be found in several works on virtual-impedance-based methods [8], [10], [12], [16]. In all of these previous works, inverters are considered as short circuit at harmonic sequences. However, nonlinear features of inverters due to dead time, voltage drop of switching devices, and nonideal switching waveforms may be hardly negligible, even when an output voltage closed loop is incorporated [11]. Moreover, the output voltage closed loop may be omitted in inverter control methods providing virtual inertia, such as synchronverter [28] and virtual synchronous generator (VSG) [29]–[30], which inherit the advantages of conventional droop control, and provide inertia support for the system [31]. As these methods focus on mimicking the behavior of a synchronous generator, multi inner loops may influence the desired dynamic performance. Moreover, the absence of the output voltage loop simplifies the control system of the inverter, otherwise complicated tuning of cascaded controllers should be performed [32]. However, this absence of the output voltage loop makes these control methods more sensitive to nonlinearities of inverters.

In view of aforementioned new findings in recent years, it may be no longer appropriate to consider inverters as short circuit at harmonic sequences. As the major nonlinearity of inverters comes from the dead time, and the effect of the dead time can be modeled as voltage sources at each harmonic sequence [11], voltage sources $\boldsymbol{V}^n_{\text{disk}}$ $(k = 1, 2)$ are added in Fig. 3 to model nonlinearities of inverters.

From Fig. 3, it can be noticed that if $\boldsymbol{V}^n_{\text{disk}}$ are nearly $\boldsymbol{0}$, and $|\boldsymbol{Z}^n_{\text{line}k} + \boldsymbol{Z}^n_{\text{inv}k}|$ are small, $\boldsymbol{V}^n_{\text{bus}}$ will become small. If $\boldsymbol{Z}^n_{\text{line}k} + \boldsymbol{Z}^n_{\text{inv}k}$ are further reshaped inversely proportional to power ratings of inverters, $\boldsymbol{I}^n_{\text{dis}}$ can be shared among $\boldsymbol{I}^n_{\text{out}k}$ according to the power rating ratio of inverters. This is the basic idea of the methods based on negative virtual impedance [9], [10], [12]. However, if $\boldsymbol{V}^n_{\text{disk}}$ are not negligible, small $|\boldsymbol{Z}^n_{\text{line}k} + \boldsymbol{Z}^n_{\text{inv}k}|$ will make $\boldsymbol{V}^n_{\text{bus}}$ prone to be polluted by $\boldsymbol{V}^n_{\text{disk}}$. Moreover, small $|\boldsymbol{Z}^n_{\text{line}k} + \boldsymbol{Z}^n_{\text{inv}k}|$ implies short circuit between two voltage sources $\boldsymbol{V}^n_{\text{dis1}}$ and $\boldsymbol{V}^n_{\text{dis2}}$, which results in large circulating harmonic currents, even when the load does not generate any harmonic currents $(\boldsymbol{I}^n_{\text{dis}} = \boldsymbol{0})$. Therefore, large $|\boldsymbol{Z}^n_{\text{line}k} + \boldsymbol{Z}^n_{\text{inv}k}|$ are preferable in this case [11]. However, in this case, if $\boldsymbol{I}^n_{\text{dis}}$ is considerable, $\boldsymbol{V}^n_{\text{bus}}$ may become larger due to amplified voltage drop on $|\boldsymbol{Z}^n_{\text{line}k} + \boldsymbol{Z}^n_{\text{inv}k}|$.

It can be concluded that negative virtual impedance will amplify the harmonic current caused by inverter nonlinearities, and positive virtual impedance will deteriorate the bus voltage quality. Therefore, in the case that the bus voltage quality and current sharing are required, whereas inverter nonlinearities are not negligible, there is no proper design of the conventional virtual-impedance-based methods, as both negative and positive virtual impedance are not appropriate. As a result, a new solution is expected.

III. Proposed Control Scheme

The proposed control scheme embedded in inverter-interfaced DGs is shown in Fig. 4. It is composed of two parts: the power

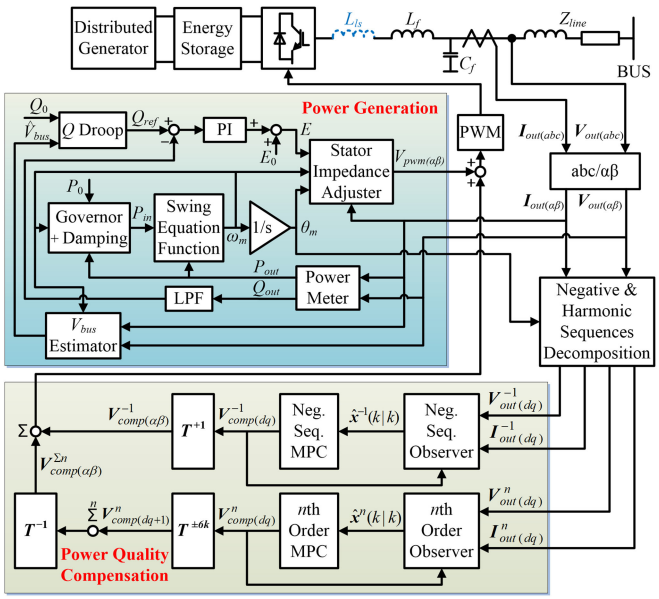

Fig. 4. Proposed control scheme of inverter-interfaced DGs.

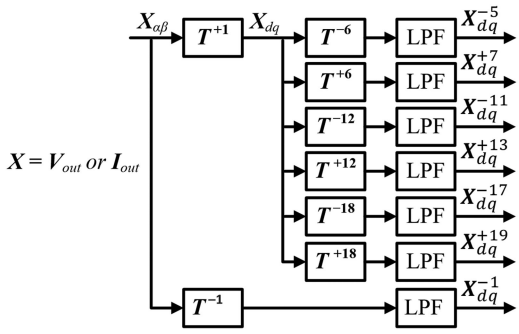

Fig. 5. Negative and harmonic sequences decomposition block.

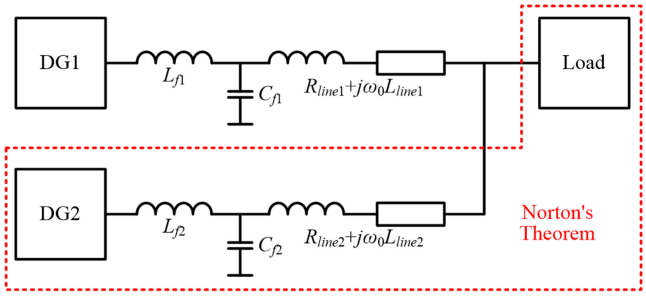

Fig. 6. Equivalent circuit of the studied microgrid at nth-order sequence.

generation part controls the voltage, frequency, active, and reactive power of the DGs; and the power quality compensation part is responsible for the bus voltage compensation and compensation current sharing. The power generation part adopted in this paper is a VSG control [30]. As mentioned in Section II, this control method is relatively sensitive to nonlinearities of inverters due to the absence of the output voltage control loop, thus, negative-virtual-impedance-based methods are not effective in this control scheme. Contrarily, the proposed power quality compensation part is compatible with other existing decentralized control methods for parallel inverters, e.g., conventional droop control [33], [34]. Nevertheless, the power generation control part is beyond the scope of this paper.

The power quality compensation part is composed of state observers and MPCs for fundamental negative sequence and each harmonic sequence to realize the proposed cost-function-based method. In this paper, -5th-, $+7$th-, -11th-, $+13$th-, -17th-, and $+19$th-order harmonics are involved in the control scheme, as they are dominant harmonic sequences under balanced loading condition. Although in the case of unbalanced loading, $+5$th, -7th, $+11$th, -13th, $+17$th, and -19th-order harmonics may also appear, they are generally much smaller compared to the controlled ones. The design methods of observers and MPCs are discussed in Section IV.

The negative and harmonic sequences for the power quality compensation part are obtained from the negative and harmonic sequences decomposition block shown in Fig. 5. This decomposition method is based on the well-known multiple synchronous harmonic dq transformations [35]. The transformation matrices $\boldsymbol{T}^{\pm \boldsymbol{n}}$ are defined as (1), and the low-pass filters (LPFs) are second-order filters with cutoff frequency at 40 Hz and damping ratio ζ at 0.8

$$\boldsymbol{T}^{\pm \boldsymbol{n}} = \boldsymbol{T}\left(\pm n\theta_m\right) = \begin{bmatrix} \cos \pm n\theta_m & \sin \pm n\theta_m \\ -\sin \pm n\theta_m & \cos \pm n\theta_m \end{bmatrix}. \quad (1)$$

IV. Design of Observers and MPCs

A. State-Space Models of the Plants

First, in order to apply MPCs to realize the proposed cost-function-based control, plant models should be built. As shown in Section III, each sequence is studied and controlled separately according to the well-known superposition theorem in this paper. Fig. 6 shows the equivalent circuit of Fig. 2 at the nth-order sequence. It is noteworthy that in order to simplify the expression of following equations, the grid-side inductor of the *LCL* filter is merged into line inductance L_{line}.

As shown in Fig. 6, the rest part of the microgrid seen from each DG, including other generators and loads, can be modeled as a Norton's equivalent circuit connected to the ac bus. Therefore, although grid-connected operation is not discussed in this paper due to the page limit, it is straightforward that the proposed method also works well in a grid-connected mode, because the grid can also be considered as a part of the Norton's equivalent circuit. Generally, the power quality of the microgrid in a grid-connected mode is less of an issue owing to the presence of a stiff voltage source. Moreover, the proposed method can be easily applied to a multiple-bus microgrid. In this case, each bus can be considered as a sub-microgrid, and thus, the proposed control can be applied to each individual bus to which at least one inverter-interfaced DG is connected. It is also noteworthy that the proposed power quality compensation control can be applied to only a part of DGs connected to the concerned bus. In this case, only DGs equipped with the proposed control generate negative and harmonic sequences current and the other DGs generate pure positive fundamental sequence current at steady state. Therefore, inverter-interfaced DG with the

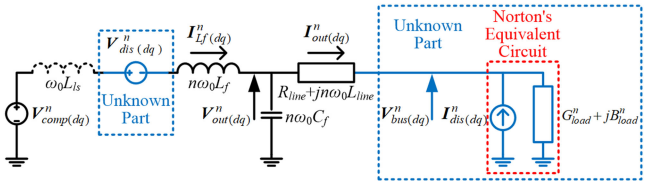

Fig. 7. Equivalent circuit model of each DG at nth-order sequence.

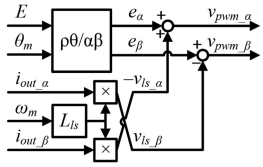

Fig. 8. Stator impedance adjuster in the power generation part.

proposed control can prevent rotating machines (both motors and generators) connected to the same ac bus from negative and harmonic sequences current.

The resulted equivalent circuit for the studied DG is shown in Fig. 7. The load admittance $G^n_{\text{load}} + jB^n_{\text{load}}$ is unknown and the bus voltage $\boldsymbol{V}^n_{\text{bus}(dq)}$, the disturbance current $\boldsymbol{I}^n_{\text{dis}(dq)}$ and the disturbance voltage $\boldsymbol{V}^n_{\text{dis}(dq)}$ caused by nonlinearities of the inverter are considered as unmeasurable variables. Inverter nonlinearities are modeled as voltage source because they mainly result from dead time. As some other nonlinearities such as voltage drop of switching devices and non-ideal switching waveforms are also influenced by current, generally, $\boldsymbol{V}^n_{\text{dis}(dq)}$, as long as other unmeasurable variables, may vary according to loading condition.

Using Kirchhoff's circuit laws, following equations can be obtained:

$$L_f \frac{\mathrm{d}i^n_{Lfd}}{\mathrm{d}t} = n\omega_0 L_f i^n_{Lfq} + \omega_0 L_{ls} i^n_{\text{out}q} + v^n_{\text{comp}d} - v^n_{\text{dis}d} - v^n_{\text{out}d} \tag{2}$$

$$L_f \frac{\mathrm{d}i^n_{Lfq}}{\mathrm{d}t} = -n\omega_0 L_f i^n_{Lfd} - \omega_0 L_{ls} i^n_{\text{out}d} + v^n_{\text{comp}q} - v^n_{\text{dis}q} - v^n_{\text{out}q} \tag{3}$$

$$C_f \frac{\mathrm{d}v^n_{\text{out}d}}{\mathrm{d}t} = n\omega_0 C_f v^n_{\text{out}q} + i^n_{Lfd} - i^n_{\text{out}d} \tag{4}$$

$$C_f \frac{\mathrm{d}v^n_{\text{out}q}}{\mathrm{d}t} = -n\omega_0 C_f v^n_{\text{out}d} + i^n_{Lfq} - i^n_{\text{out}q} \tag{5}$$

$$L_{\text{line}} \frac{\mathrm{d}i^n_{\text{out}d}}{\mathrm{d}t} = -R_{\text{line}} i^n_{\text{out}d} + n\omega_0 L_{\text{line}} i^n_{\text{out}q} + v^n_{\text{out}d} - v^n_{\text{bus}d} \tag{6}$$

$$L_{\text{line}} \frac{\mathrm{d}i^n_{\text{out}q}}{\mathrm{d}t} = -R_{\text{line}} i^n_{\text{out}q} - n\omega_0 L_{\text{line}} i^n_{\text{out}d} + v^n_{\text{out}q} - v^n_{\text{bus}q} \tag{7}$$

$$G^n_{\text{load}} v^n_{\text{bus}d} - B^n_{\text{load}}\, v^n_{\text{bus}q} = i^n_{\text{out}d} + i^n_{\text{dis}d} \tag{8}$$

$$G^n_{\text{load}} v^n_{\text{bus}q} + B^n_{\text{load}}\, v^n_{\text{bus}d} = i^n_{\text{out}q} + i^n_{\text{dis}q} \tag{9}$$

where L_{ls} is the virtual inductance applied in the stator impedance adjuster of the power generation control part [29], as shown in Fig. 8, and other parameters are defined in Fig. 7. It is noteworthy that the virtual inductance L_{ls} is designed only for improving the performance of the power generation part and is not related to the proposed power quality compensation part. However, this virtual impedance control changes the plant model of all sequences, thus its influence should be taken into consideration.

It should be noticed that C_f and L_{line} are usually very small. These small coefficients of derivative terms lead to very small eigenvalues, which cannot be handled with MPC executed at 10∼20 kHz, which is the typical control frequency for inverter-based DGs. Therefore, derivative terms of $C_f \frac{d}{dt}$ and $L_{\text{line}} \frac{d}{dt}$ in (4)–(7) should be neglected as shown in (10)–(13)

$$0 = n\omega_0 C_f v^n_{\text{out}q} + i^n_{Lfd} - i^n_{\text{out}d} \tag{10}$$

$$0 = -n\omega_0 C_f v^n_{\text{out}d} + i^n_{Lfq} - i^n_{\text{out}q} \tag{11}$$

$$0 = -R_{\text{line}} i^n_{\text{out}d} + n\omega_0 L_{\text{line}} i^n_{\text{out}q} + v^n_{\text{out}d} - v^n_{\text{bus}d} \tag{12}$$

$$0 = -R_{\text{line}} i^n_{\text{out}q} - n\omega_0 L_{\text{line}} i^n_{\text{out}d} + v^n_{\text{out}q} - v^n_{\text{bus}q}. \tag{13}$$

It is also noteworthy that equivalent series resistances of C_f and L_f are neglected in Fig. 7 and related equations. This simplifies the plant models and will not deteriorate control accuracy, as the disturbance models and the observers discussed later in this section will mitigate the mismatch between the supposed plant models and the real ones.

From (2), (3) and (8)–(13), the state-space models of the plants can be obtained as

$$\begin{cases} \dot{\boldsymbol{x}}_p(t) = \boldsymbol{A}_t \boldsymbol{x}_p(t) + \boldsymbol{B}_t u(t) + \boldsymbol{E}_t \boldsymbol{w}_p(t) \\ y(t) = \boldsymbol{C}_p\, \boldsymbol{x}_p(t) + \boldsymbol{F}_p \boldsymbol{w}_p(t) \end{cases} \tag{14}$$

where state vector $\boldsymbol{x}_p = [\, i^n_{Lfd}\ i^n_{Lfq}\,]^{\mathrm{T}}$, output vector $\boldsymbol{y} = [\, v^n_{\text{out}d}\ v^n_{\text{out}q}\ i^n_{\text{out}d}\ i^n_{\text{out}q}\ v^n_{\text{bus}d}\ v^n_{\text{bus}q}\,]^{\mathrm{T}}$, control input vector $\boldsymbol{u} = [\, v^n_{\text{comp}d}\ v^n_{\text{comp}q}\,]^{\mathrm{T}}$, disturbance input vector $\boldsymbol{w}_p = [\, v^n_{\text{dis}d}\ v^n_{\text{dis}q}\ i^n_{\text{dis}d}\ i^n_{\text{dis}q}\,]^{\mathrm{T}}$, t indicates the time, and matrices are shown as follows:

$$\boldsymbol{A}_t = \begin{bmatrix} \frac{-C_{x11} + \omega_0 L_{ls} C_{x41}}{L_f} & \frac{n\omega_0 L_f - C_{x12} + \omega_0 L_{ls} C_{x42}}{L_f} \\ -\frac{n\omega_0 L_f + C_{x21} + \omega_0 L_{ls} C_{x31}}{L_f} & -\frac{C_{x22} + \omega_0 L_{ls} C_{x32}}{L_f} \end{bmatrix} \tag{15}$$

$$\boldsymbol{B}_t = \begin{bmatrix} \frac{1}{L_f} & 0 \\ 0 & \frac{1}{L_f} \end{bmatrix} \tag{16}$$

$$\boldsymbol{E}_t = \begin{bmatrix} -\frac{1}{L_f} & 0 & \frac{-C_{x13} + \omega_0 L_{ls} C_{x43}}{L_f} & \frac{-C_{x14} + \omega_0 L_{ls} C_{x44}}{L_f} \\ 0 & -\frac{1}{L_f} & -\frac{C_{x23} + \omega_0 L_{ls} C_{x33}}{L_f} & -\frac{C_{x24} + \omega_0 L_{ls} C_{x34}}{L_f} \end{bmatrix} \tag{17}$$

$$\boldsymbol{C}_p = \begin{bmatrix} C_{x11} & C_{x12} \\ C_{x21} & C_{x22} \\ C_{x31} & C_{x32} \\ C_{x41} & C_{x42} \\ C_{x51} & C_{x52} \\ C_{x61} & C_{x62} \end{bmatrix} \tag{18}$$

$$\boldsymbol{F}_p = \begin{bmatrix} 0 & 0 & C_{x13} & C_{x14} \\ 0 & 0 & C_{x23} & C_{x24} \\ 0 & 0 & C_{x33} & C_{x34} \\ 0 & 0 & C_{x43} & C_{x44} \\ 0 & 0 & C_{x53} & C_{x54} \\ 0 & 0 & C_{x63} & C_{x64} \end{bmatrix} \tag{19}$$

where C_{xij} is the element in the ith row and jth column of the matrix $\boldsymbol{C}_x = {\boldsymbol{A}_x}^{-1}\boldsymbol{B}_x$, where $\boldsymbol{A}_x$ and $\boldsymbol{B}_x$ are shown as follows:

$$\boldsymbol{A}_x = \begin{bmatrix} 0 & n\omega_0 C_f & -1 & 0 & 0 & 0 \\ -n\omega_0 C_f & 0 & 0 & -1 & 0 & 0 \\ 1 & 0 & -R_{\text{line}} & n\omega_0 L_{\text{line}} & -1 & 0 \\ 0 & 1 & -n\omega_0 L_{\text{line}} & -R_{\text{line}} & 0 & -1 \\ 0 & 0 & -1 & 0 & G^n_{\text{load}} & -B^n_{\text{load}} \\ 0 & 0 & 0 & -1 & B^n_{\text{load}} & G^n_{\text{load}} \end{bmatrix} \tag{20}$$

$$\boldsymbol{B}_x = \begin{bmatrix} -1 & 0 & 0 & 0 \\ 0 & -1 & 0 & 0 \\ 0 & 0 & 0 & 0 \\ 0 & 0 & 0 & 0 \\ 0 & 0 & 1 & 0 \\ 0 & 0 & 0 & 1 \end{bmatrix}. \tag{21}$$

It is remarkable that the second-order LPFs used in the feedback paths of the proposed control scheme shown in Fig. 5 are not included in the state-space model shown in (14), otherwise these second-order filters will introduce eight additional state variables that largely increase the computational complexity of the observers and MPCs. This neglect simplifies the design of observers and MPCs, and its influence on closed-loop stability and dynamic performance can be eliminated by the proper tuning of MPCs as discussed in Section V-B.

Using the backward Euler method, (14) can be discretized as

$$\begin{cases} \boldsymbol{x}_p\ (k+1) = \boldsymbol{A}_p\ \boldsymbol{x}_p(k) + \boldsymbol{B}_p u(k) + \boldsymbol{E}_p \boldsymbol{w}_p(k) \\ y(k)\ = \boldsymbol{C}_p\ \boldsymbol{x}_p(k) + \boldsymbol{F}_p \boldsymbol{w}_p(k) \end{cases} \tag{22}$$

where $\boldsymbol{A}_p = \boldsymbol{I} + T_s \boldsymbol{A}_t$, $\boldsymbol{B}_p = T_s\ \boldsymbol{B}_t$, $\boldsymbol{E}_p = T_s\ \boldsymbol{E}_t$, $\boldsymbol{I}$ is the identity matrix, T_s is the sampling and control period of controller, and k indicates discrete-time sequence.

In order to estimate the disturbances caused by the unknown nonlinearities of the inverter, Norton's equivalent circuits and parameters mismatch, the following four-dimensional disturbance models are added into the state-space models of the plants:

$$\begin{cases} \boldsymbol{x}_{\text{dis}}(k+1) = \boldsymbol{A}_{\text{dis}}\ \boldsymbol{x}_{\text{dis}}(k) + \boldsymbol{B}_{\text{dis}} \boldsymbol{w}_{\text{dis}}(k) \\ \boldsymbol{w}_p(k)\ = \boldsymbol{C}_{\text{dis}}\ \boldsymbol{x}_{\text{dis}}(k) + \boldsymbol{D}_{\text{dis}} \boldsymbol{w}_{\text{dis}}(k) \end{cases} \tag{23}$$

where $\boldsymbol{A}_{\text{dis}} = \boldsymbol{B}_{\text{dis}}\ = \boldsymbol{C}_{\text{dis}}\ =\ \boldsymbol{I}$ and $\boldsymbol{D}_{\text{dis}} =\ \boldsymbol{0}$, and $\boldsymbol{w}_{\text{dis}}$ are Gaussian noises related to unknown plant disturbances.

TABLE I
PARAMETERS OF THE POWER GENERATION PART

Parameter	Value	Parameter	Value
S_{base1}	5 kVA	$T_{fq1} = T_{fq2}$	7.96×10^{-3} s
S_{base2}	2.5 kVA	$K^*_{pq1} = K^*_{pq2}$	0.005 pu
V_{base}	200 V	$T_{iq1} = T_{iq2}$	1.25×10^{-4} s
ω_0	376.99 rad/s	$k^*_{x\omega1} = k^*_{x\omega2}$	156.27 pu
$P^*_{01} = P^*_{02}$	1 pu	$k^*_{xP1} = k^*_{xP2}$	14.362 pu
$Q^*_{01} = Q^*_{02}$	0 pu	$k^*_{xI1} = k^*_{xI2}$	110.17 pu
$M^*_1 = M^*_2$	8 s	L_{ls1}	3.436 mH
$k^*_{p1} = k^*_{p2}$	20 pu	L_{ls2}	7.902 mH
$k^*_{q1} = k^*_{q2}$	10 pu		

Substitute (23) into (22), the complete plant models can be expressed as

$$\begin{cases} x(k+1) =\ Ax(k) + Bu(k) + E\boldsymbol{w}_{\text{dis}}(k) \\ y\ (k) =\ Cx(k) + F\boldsymbol{w}_{\text{dis}}(k) \end{cases} \tag{24}$$

where $\boldsymbol{x} = \left[\begin{smallmatrix} \boldsymbol{x}_p \\ \boldsymbol{x}_{\text{dis}} \end{smallmatrix}\right]$, $\boldsymbol{A} = \left[\begin{smallmatrix} \boldsymbol{A}_p & \boldsymbol{E}_p\boldsymbol{C}_{\text{dis}} \\ \boldsymbol{0} & \boldsymbol{A}_{\text{dis}} \end{smallmatrix}\right]$, $\boldsymbol{B} = \left[\begin{smallmatrix} \boldsymbol{B}_p \\ \boldsymbol{0} \end{smallmatrix}\right]$, $\boldsymbol{E} = \left[\begin{smallmatrix} \boldsymbol{E}_p\boldsymbol{D}_{\text{dis}} \\ \boldsymbol{B}_{\text{dis}} \end{smallmatrix}\right]$, $\boldsymbol{C} = \left[\boldsymbol{C}_p\ \boldsymbol{F}_p\boldsymbol{C}_{\text{dis}}\right]$, and $\boldsymbol{F} = \boldsymbol{F}_p\ \boldsymbol{D}_{\text{dis}}$.

It is noteworthy that from (23), $\boldsymbol{x}_{\text{dis}} = \boldsymbol{w}_p\ = [v^n_{\text{disd}}\ v^n_{\text{disq}}\ i^n_{\text{disd}}\ i^n_{\text{disq}}]^{\text{T}}$. That is to say, the main disturbances in Fig. 7, i.e., nonlinearities of the inverter and disturbance current of Norton's circuit are included into the state variables in the complete plant models as shown in (24). Therefore, it is possible to use observers to estimate these disturbances as discussed in the following section. It is noteworthy that as mentioned previously, these disturbances may vary according to loading conditions; however, these variations will be quickly detected by the observers. Besides, whenever there is a parameter mismatch between the supposed plant and the real plant, it will also be corrected by the disturbance model owing to the presence of observers [24]. With this effort, the proposed method is very insensitive to unknown disturbances and plant uncertainties, thus, its control accuracy can be significantly improved. In particular, nonlinearities of inverters, which cannot be well handled by virtual-impedance-based methods, can be easily estimated by the observers. As their impacts are well considered in (2) and (3) during the plant modeling, the effectiveness of the proposed control is immune to the existence of these nonlinearities.

B. Design of the State Observers

It is noteworthy that not all output variable in $\boldsymbol{y}$ is measurable as the bus voltage is assumed to be unknown. Therefore, the output equations of (24) can be rewritten as follows for measurable output variables:

$$\boldsymbol{y}_m(k) = \boldsymbol{C}_m \boldsymbol{x}(k) + \boldsymbol{F}_m \boldsymbol{w}_{\text{dis}}(k) + \boldsymbol{w}_m(k) \tag{25}$$

where $\boldsymbol{y}_m = [\,v^n_{\text{out}d}\ v^n_{\text{out}q}\ i^n_{\text{out}d}\ i^n_{\text{out}q}\,]^{\text{T}}$, $\boldsymbol{C}_m$ and $\boldsymbol{F}_m$ are the submatrices of $\boldsymbol{C}$ and $\boldsymbol{F}$ related to $\boldsymbol{y}_m$, and $\boldsymbol{w}_m$ is a Gaussian noise related to the measurement uncertainty.

Based on (24) and (25), the state vectors can be observed using the Kalman filter as follows:

$$\hat{\boldsymbol{x}}\,(k|k) = \hat{\boldsymbol{x}}\,(k|k-1) + \boldsymbol{M}(\boldsymbol{y}_m(k) - \hat{\boldsymbol{y}}_m\,(k|k-1)) \quad (26)$$

where $\hat{\boldsymbol{x}}(k|k-1)$ indicates the predicted $\boldsymbol{x}$ at k based on the information at $k-1$, and $\boldsymbol{M}$ is the Kalman gain matrix, which can be calculated from (24) and (25) as shown in [36].

From (24)–(26), the updated state estimates are deduced as

$$\hat{\boldsymbol{x}}\,(k|k) = \boldsymbol{A}_k\,\hat{\boldsymbol{x}}(k-1|k-1) + \boldsymbol{B}_k\boldsymbol{u}(k-1) + \boldsymbol{M}\boldsymbol{y}_m(k) \quad (27)$$

where $\boldsymbol{A}_k = \boldsymbol{A} - \boldsymbol{M}\boldsymbol{C}_m\boldsymbol{A}$ and $\boldsymbol{B}_k = \boldsymbol{B} - \boldsymbol{M}\boldsymbol{C}_m\boldsymbol{B}$. All these matrices can be obtained through offline calculation.

As $\boldsymbol{A}_k$, $\boldsymbol{B}_k$, and $\boldsymbol{M}$ are 6×6, 6×2, and 6×4 matrices, respectively, the online computational complexity of one state observer is equivalent to 72 multiplications and 66 additions per control period.

C. Design of the MPCs

The principle of the proposed control lies in the cost functions, which is optimized by the MPCs. In order to compensate the bus voltage power quality and share current sequences, simultaneously, the cost functions of the MPCs are proposed as

$$J(k) = \sum_{j=N_1}^{N_2} \|\hat{\boldsymbol{y}}_o\,(k+j|k) - \boldsymbol{r}\,(k+j)\|^2_{\boldsymbol{Q}(j)} + \sum_{j=1}^{N_3} \|\boldsymbol{u}\,(k+j-1)\|^2_{\boldsymbol{R}(j)} \quad (28)$$

where expression $\|\boldsymbol{X}\|^2_{\boldsymbol{Q}} = \boldsymbol{X}^{\mathrm{T}}\,\boldsymbol{Q}\boldsymbol{X}$ is the compact representation of quadratic form, N_1 and N_2 are the start and the final steps of the prediction horizon, respectively, N_3 is the control horizon, $\hat{\boldsymbol{y}}_o = [\,\hat{i}^n_{\mathrm{outd}}\ \hat{i}^n_{\mathrm{outq}}\ \hat{v}^n_{\mathrm{busd}}\ \hat{v}^n_{\mathrm{busq}}\,]^T$ is the output variables to be controlled by MPC, $\boldsymbol{r}$ is the reference trajectory of $\hat{\boldsymbol{y}}_o$, which is set to $\boldsymbol{0}$ in this study, $\Delta\boldsymbol{u}(k) = \boldsymbol{u}(k) - \boldsymbol{u}(k-1)$ is the variation of the control input vector, and $\boldsymbol{Q}(j) = \mathrm{diag}(Q^n_I, Q^n_I, Q^n_V, Q^n_V)$ and $\boldsymbol{R}(j) = \mathrm{diag}(R^n_u, R^n_u)$ are weighting matrices for the output variables and control variables, respectively.

It can be interpreted that the cost functions (28) try to minimize the negative/harmonic sequences of the bus voltage and the inverter output current. Therefore, if these cost functions are applied to all the controlled sequences in all studied inverters, an equilibrium operating point minimizing these voltage and current sequences will be achieved automatically. As for the proper sharing of current sequences, proper tuning of $\boldsymbol{Q}(j)$ discussed in next section is the key.

In the presented work, general MPC without constrain is adopted on account of its relatively lower online computational complexity. Therefore, the MPC algorithms can be deduced as follows:

$$\boldsymbol{u}(k) = \boldsymbol{K_x}\,\hat{\boldsymbol{x}}\,(k|k) + (\boldsymbol{I} + \boldsymbol{K_u})\boldsymbol{u}\,(k-1) \quad (29)$$

where $\boldsymbol{K_x}$ and $\boldsymbol{K_u}$ are feedback gain matrices of state and control variables, respectively. To simplify the online computation, they can be calculated offline from the cost functions (28) and the state-space equations (24) using the method explained in [37].

As $\boldsymbol{K_x}$ and $(\boldsymbol{I} + \boldsymbol{K_u})$ are 2×6 and 2×2 matrices, respectively, and elements K_{x14}, K_{x23}, K_{u12}, and K_{u21} are all 0, the online computational complexity of one MPC is equivalent to 12 multiplications and 10 additions per control period.

TABLE II
PARAMETERS OF THE POWER QUALITY COMPENSATION PART

Parameter	Value	Parameter	Value
N_1	1	N_3	3
N_2	20		
k_h^{-1}	0.1	R_u^{-1}	20000 V^{-2}
k_h^{-5}	0.05	R_u^{-5}	5000 V^{-2}
k_h^{+7}	0.1	R_u^{+7}	4000 V^{-2}
k_h^{-11}	0.2	R_u^{-11}	5000 V^{-2}
k_h^{+13}	0.2	R_u^{+13}	3000 V^{-2}
k_h^{-17}	0.5	R_u^{-17}	4000 V^{-2}
k_h^{+19}	0.5	R_u^{+19}	2000 V^{-2}
Above parameters are applied to both DG 1 and DG 2			

V. TUNING OF MPC PARAMETERS

First of all, prediction horizon $N_1 \sim N_2$ and control horizon N_3 should be long enough to assure correct prediction. As general MPC without constrain is adopted in this paper, longer prediction horizon and control horizon only complicate offline computation of $\boldsymbol{K}_x$ and $\boldsymbol{K}_u$ and do not require any additional online resources. Therefore, long horizons such as the recommended values shown in Table II can be adopted. In view of the fact that further increasing these horizons barely change $\boldsymbol{K}_x$ and $\boldsymbol{K}_u$, it can be concluded that the recommended values are longer enough for precise prediction.

Tuning of the weighting factors (Q^n_I, Q^n_V, and R^n_u) is the key of the proposed method. As the absolute values of weighting factors do not influence the control results, Q^n_V can be arbitrarily set to 1 V^{-2}, and Q^n_I and R^n_u are tuned relatively to Q^n_V.

To study the influence of weighting factors, an s-domain closed-loop model of the studied microgrid is established for pole loci analyses, as shown in Fig. 9. In Fig. 9, the plant model is an s-domain state-space model derived from circuit equations in a similar way to (14). However, at this time, the whole microgrid circuit shown in Fig. 2 is included and no simplification such as (10)–(13) is applied. The second-order LPFs shown in Fig. 5, which are neglected in Section IV-A, are also included for the correct stability and dynamic analyses. Subscript f is added to $\boldsymbol{V}^n_{\mathrm{out}k}$ and $\boldsymbol{I}^n_{\mathrm{out}k}$ $(k = 1,\ 2)$ after LPFs, to distinguish the measured variables before and after LPFs. It is noteworthy that because LPFs, observers and MPCs are implemented in a digital controller, they are first modeled in z domain, and then, transferred to s domain using zero-order hold. With these efforts, the presented closed-loop control model is quite close to the real system. Due to the page limit, the mathematical representation of each block is omitted in this paper, and only the closed-loop pole loci are presented.

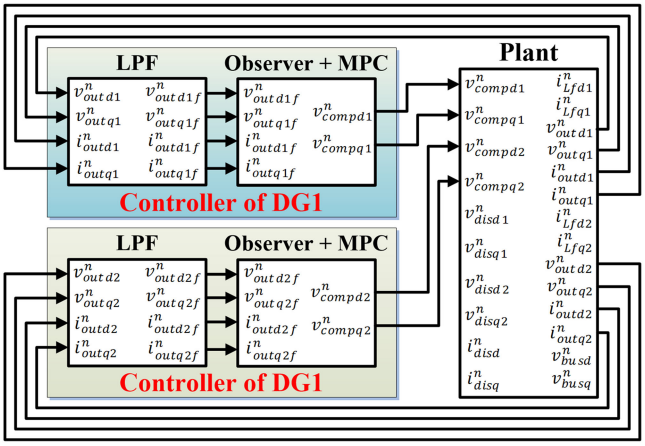

Fig. 9. Closed-loop control model of the studied microgrid at nth-order sequence.

A. Tuning of Q_I^n

The ratio of Q_I^n/Q_V^n is determined according to the tradeoff between the bus voltage steady-state error and current sharing accuracy. At steady state, the gradient of cost functions $J(k)$ in the direction of $\Delta \boldsymbol{u}(k)$ should be $\mathbf{0}$. This gives

$$\nabla_{\Delta \boldsymbol{u}(k)} J(k) = (\boldsymbol{C}_o \boldsymbol{B})^{\mathrm{T}} \boldsymbol{Q}(k+1) \hat{\boldsymbol{y}}_{\boldsymbol{o}} (k+1|k) = \mathbf{0} \quad (30)$$

where $\boldsymbol{C}_o$ is the submatrix of $\boldsymbol{C}$ related to $\hat{\boldsymbol{y}}_o$. From (30), it can be deduced that

$$Q_I^n (\boldsymbol{Y}_{\mathrm{load}}^n)^{\mathrm{T}} \hat{\boldsymbol{I}}_{\mathrm{out}(dq)}^n = -Q_V^n \hat{\boldsymbol{V}}_{\mathrm{bus}\,(dq)}^n \quad (31)$$

where $\boldsymbol{Y}_{\mathrm{load}}^n = \begin{bmatrix} G_{\mathrm{load}}^n & -B_{\mathrm{load}}^n \\ B_{\mathrm{load}}^n & G_{\mathrm{load}}^n \end{bmatrix}$ is the load admittance matrix used in state-space models. As G_{load}^n and B_{load}^n are unknown parameters, it can be assumed that $G_{\mathrm{load}}^n = S_{\mathrm{base}}/V_{\mathrm{base}}^2$ and $B_{\mathrm{load}}^n = 0$, where S_{base} is the power rating of the DG and V_{base} is the nominal voltage. Even if these assumed load admittance matrices are different from those of the real plants, control accuracy of the MPCs will not be influenced because the model mismatches are observed and compensated by the disturbance models as discussed in Section IV-A.

Assuming the acceptable error of $\|\hat{\boldsymbol{V}}_{\mathrm{bus}(dq)}^n\|$ is k_h^n pu when $\|\hat{\boldsymbol{I}}_{\mathrm{out}(dq)}^n\|$ is 1 pu. From (31)

$$Q_I^n = Q_V^n \frac{k_h^n}{(G_{\mathrm{load}}^n)^2} = Q_V^n k_h^n \frac{V_{\mathrm{base}}^4}{S_{\mathrm{base}}^2}. \quad (32)$$

From (31) and (32)

$$\begin{cases} i_{\mathrm{outd}}^n = -\frac{S_{\mathrm{base}}}{k_h^n V_{\mathrm{base}}^2} v_{\mathrm{busd}}^n \\ i_{\mathrm{outq}}^n = -\frac{S_{\mathrm{base}}}{k_h^n V_{\mathrm{base}}^2} v_{\mathrm{busq}}^n. \end{cases} \quad (33)$$

It can be observed from (33) that if k_h^n is set equally and $\hat{\boldsymbol{V}}_{\mathrm{bus}(dq)}^n$ is predicted correctly in each DG, $\hat{\boldsymbol{I}}_{\mathrm{out}(dq)}^n$ of each DG will be shared proportionally to respective power rating S_{base}. This mechanism is similar to the well-known $P-f$ droop control, as shown in Fig. 10. In the $P-f$ droop control, frequency f provides the common reference for all DGs to share the active power P. In the proposed cost-function-based method, bus

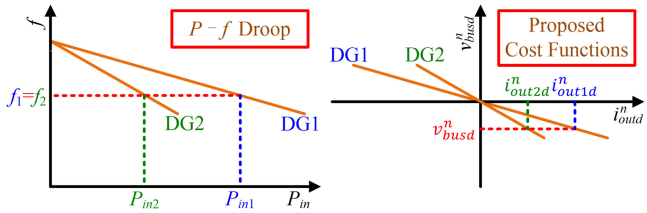

Fig. 10. Analogy of $P-f$ droop control and the proposed cost-function-based unbalance and harmonics control.

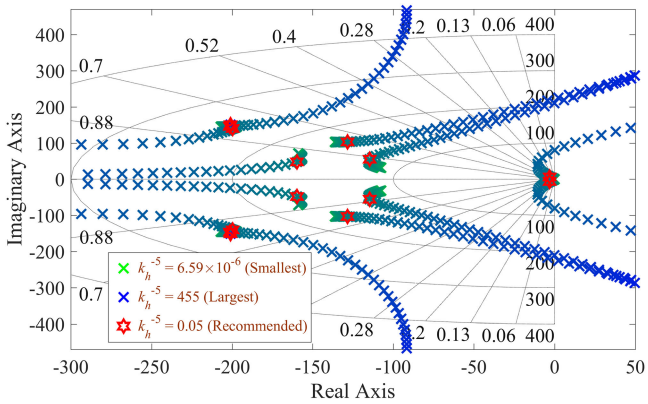

Fig. 11. Close-loop pole loci when k_h^{-5} varies (non-dominant poles out of range are not shown).

negative/harmonic voltage $\hat{\boldsymbol{V}}_{\mathrm{bus}(dq)}^n$ provides the common reference for all DGs to share the output negative/harmonic current $\hat{\boldsymbol{I}}_{\mathrm{out}(dq)}^n$.

Hence, similar to the well-known tradeoff between frequency deviation and active power sharing accuracy in $P-f$ droop control, there is also this kind of tradeoff in the proposed unbalance/harmonic control method. It can be concluded from (33) that smaller k_h^n results in smaller bus voltage harmonic/negative sequence $\hat{\boldsymbol{V}}_{\mathrm{bus}(dq)}^n$. However, the bus voltage estimation error, i.e., $\boldsymbol{\varepsilon}_{v\mathrm{bus}\,(dq)}^n = \boldsymbol{V}_{\mathrm{bus}\,(dq)}^n - \hat{\boldsymbol{V}}_{\mathrm{bus}\,(dq)}^n$, will be amplified by smaller k_h^n, resulting in a larger current sharing error $\boldsymbol{\varepsilon}_{i\mathrm{out}\,(dq)}^n$ as

$$\boldsymbol{\varepsilon}_{i\mathrm{out}\,(dq)}^n = -\frac{S_{\mathrm{base}}}{k_h^n V_{\mathrm{base}}^2} \boldsymbol{\varepsilon}_{v\mathrm{bus}\,(dq)}^n. \quad (34)$$

From (34), if k_h^n is too small, $\boldsymbol{\varepsilon}_{i\mathrm{out}\,(dq)}^n$ may become very large even when $\boldsymbol{\varepsilon}_{v\mathrm{bus}\,(dq)}^n$ is small. In this case, large circulating current at the related sequence will flow between the two inverters, no matter the magnitude of $\boldsymbol{I}_{\mathrm{dis}(dq)}^n$.

From the closed-loop pole loci shown in Fig. 11, it can also be noticed that too large k_h^n makes the system unstable, and too small k_h^n slows down the dynamic response of the system. This is because varying k_h^n not only change the Q_I^n/Q_V^n ratio, but also change the Q_I^n/R_u^n ratio. The latter plays an important role in the stability and dynamics of the current balancing, as discussed in next section. Nevertheless, this tradeoff is less important during the tuning of k_h^n, as it can be compensated by the R_u^n tuning discussed in next part. Therefore, k_h^n should be tuned first of all to balance the bus voltage steady-state error with compensation current sharing accuracy.

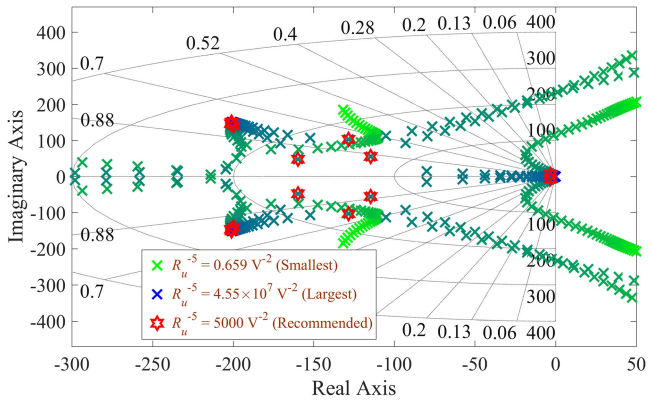

Fig. 12. Close-loop pole loci when R_u^{-5} varies (non-dominant poles out of range are not shown).

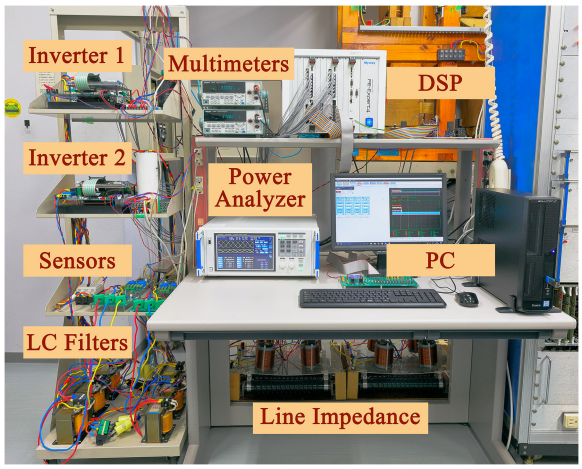

Fig. 13. Microgrid testbed for the experimental verification.

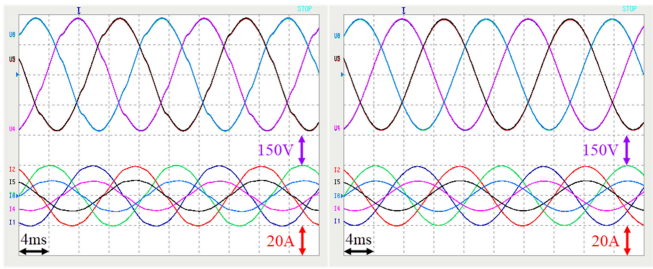

(a) (b)

Fig. 14. Bus line voltage (upper) and inverter current (lower) waveforms (a) without and (b) with the proposed power quality compensation control in Case 1.

B. Tuning of R_u^n

Tuning of R_u^n is also a tradeoff. Generally, as R_u^n penalizes the variation of the control input, smaller R_u^n leads to faster dynamic response, whereas larger R_u^n leads to a more stable and more robust closed-loop system [37]. This is also the case in the studied system, as it can be concluded from the closed-loop pole loci shown in Fig. 12. Although MPC can be tuned without penalizing the variation of control input, i.e., equivalent to dead-beat control, the proposed method is not the case because the second-order LPF is not included in the plant model, as mentioned in Section IV-A. Therefore, the closed loop should be tuned slow enough to make the LPF negligible.

Fig. 12 illustrates the optimal tuning of R_u^n. To tune the MPC as fast as possible while mitigating overshoot and oscillation, smallest R_u^n that makes damping ratio ζ (indicated by the radial lines in Fig. 12) of all dominant poles larger than 0.7 is recommended.

Finally, all control parameters of the power generation part and power quality compensation part adopted in this paper are shown in Tables I and II, respectively. Definitions of the parameters in Table I are explained in [29] and [30].

VI. Implementation of the Proposed Method

1) Model the plants using the Norton's equivalent circuits shown in Fig. 7, and finally, establish the discretized state-space equations (24). It is noteworthy that only the parameters of the *LCL* filter and line impedance are required for this modeling, and load admittance can be assumed as $G_{\text{load}}^n = S_{\text{base}}/V_{\text{base}}^2$ and $B_{\text{load}}^n = 0$. Parameter mismatch is tolerated because of the presence of disturbance models and observers.
2) Design the algorithms of state observers (27) using the Kalman filter. Gain matrices in (27) can be obtained from state-space equations (24) and (25) through offline calculation as shown in [36].
3) Design the algorithms of state feedback controllers (29) using MPC. Gain matrices in (29) can be obtained from cost functions (28) and state-space equations (24) through offline calculation as shown in [37].
4) Tune weighting factors Q_I^n and R_u^n based on the discussion in Section V. Q_I^n should be tuned to balance the bus voltage steady-state error with compensation current sharing accuracy as shown in Fig. 10, and R_u^n should be tuned to balance the dynamic response with stability using eigenvalue loci analyses similar to Fig. 12. Other parameters of MPCs can be set as typical values shown in Table II.
5) Implement the proposed power quality compensation control as shown in Fig. 4, with the algorithms of observers and MPCs obtained in the previous steps.

VII. Experimental Results

To verify the proposed decentralized control of unbalance and harmonics, experimental tests of the studied microgrid shown in Fig. 2 are performed using the setup shown in Fig. 13. Both inverters are based on intelligent power modules Mitsubishi PM75RSD060, and are controlled independently by a digital control unit Myway PE-Expert IV, in which a TI TMS320C6657 1.25-GHz dual core DSP is embedded. Due to the slow $\mathrm{d}V/\mathrm{d}t$ of Mitsubishi PM75RSD060, a relatively large dead time of 3.5 μs is added to the PWM waves of both inverters. Therefore, nonlinearities of inverters are hardly to be neglected in the studied cases. As a result, it is difficult to apply conventional virtual-impedance-based methods to this system.

The voltage/current waveforms, RMS values, unbalance ratios, and harmonic distortions are measured by a Hioki

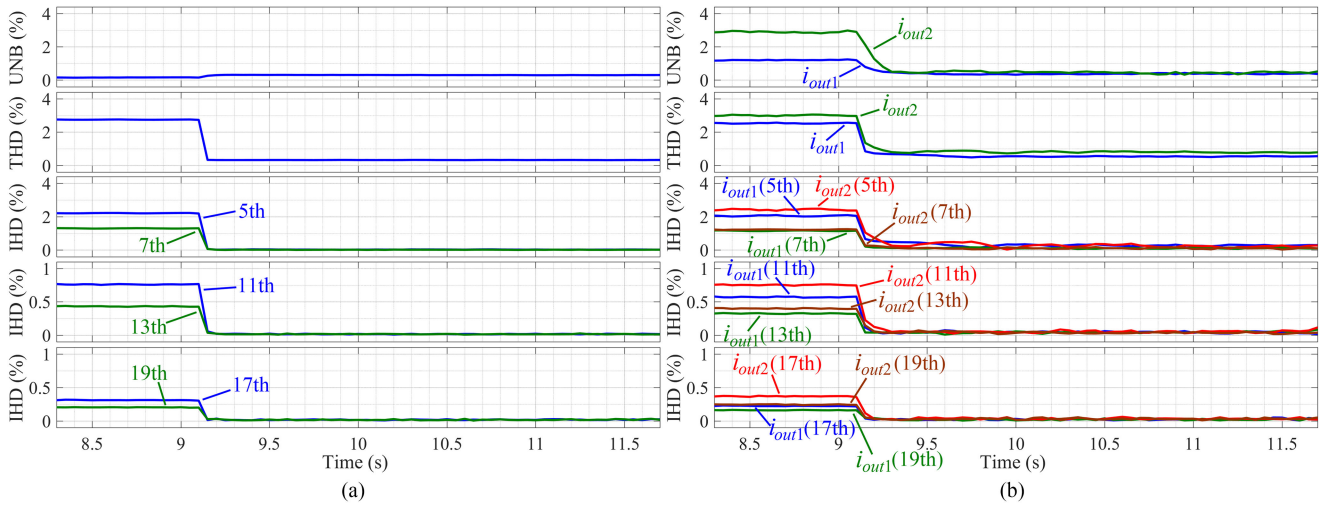

Fig. 15. UNB factors, THDs, and IHDs of (a) bus voltage and (b) inverter current when the proposed power quality compensation control is activated in Case 1.

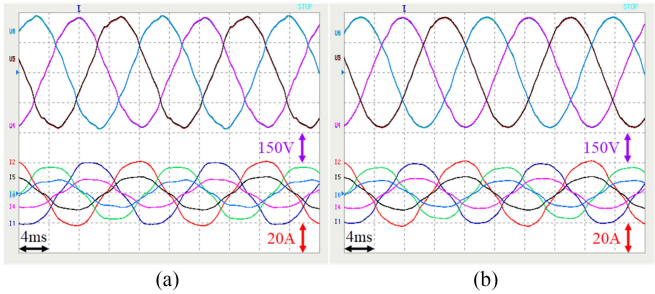

Fig. 16. Bus line voltage (upper) and inverter current (lower) waveforms (a) without and (b) with the proposed power quality compensation control in Case 2.

PW6001 power analyzer. Sampling time of the data recorder of PW6001 is set as 50 ms, and the total harmonic distortions (THDs) presented in this paper are measured up to the 100th order.

Three case studies are conducted to verify the effectiveness of the proposed method. In Case 1, only the 3P balanced *RL* load consuming 6.89 kW, 1.73 kvar is connected to the ac bus. In Case 2, all the three types of loads shown in Fig. 2 are connected, among which the 3P *RL* load consumes 4.30 kW, 1.65 kvar, and the 2P *RL* load consumes 0.98 kW, 0.07 kvar. In these two cases, the waveforms without and with the proposed control are compared, and the transient response after the activation of the proposed power quality compensation control is investigated. In Case 3, the load settings are the same as those of Case 2, whereas the performance of the proposed control during load transients is evaluated.

A. Case 1: Balanced RL Load

In the case of the balanced linear load, both bus voltage and inverter current should be balanced and sinusoidal. However, if the proposed power quality compensation control is not applied, due to nonlinearities of inverters, the voltage at inverter terminals is distorted, and this distortion causes circulating harmonic currents, which also deteriorate bus voltage waveforms, as it is shown in Fig. 14(a). When the proposed control is applied, these distortions are well controlled as shown in Fig. 14(b), because the cost functions (28) try to find the equilibrium point minimizing the harmonic sequences of the bus voltage and of the inverter output current. It is noteworthy that if negative-virtual-impedance-based methods are applied, the current waveform will getting even worse, because harmonic current sequences will be amplified due to reduced impedance between inverters.

Fig. 15 illustrates unbalance (UNB) factors, THDs, and individual harmonic distortions (IHDs) during the transient state when the proposed control is activated at around 9.1 s. It can be noticed that although the dynamic response of the MPCs is limited by the LPFs, as discussed in Section V-B, the proposed control is fast enough as the steady state is reached within 0.1 s for the bus voltage and within 0.3 s for the inverter current. It can also be concluded that the harmonics caused by nonlinearities of inverters are well compensated by the proposed control, as all the controlled harmonic orders are largely reduced in both bus voltage and inverter output current. This results in a reduction of THD from 2.75%, 2.54%, and 3.01% to 0.32%, 0.53%, and 0.80% for the bus voltage and the output current of Inverters 1 and 2, respectively. This result coincides well with the waveforms shown in Fig. 14.

B. Case 2: Complex Load

In Case 2, the control of unbalance and harmonics becomes more challenging due to the presence of unbalanced load and nonlinear load. The ideal result is that the bus voltage is balanced and sinusoidal, and the unbalanced and harmonic current is shared between inverters according to their power rating ratio. It is difficult to achieve this objective without the proposed power quality compensation method, as illustrated by the waveforms of the bus voltage and inverter output current shown in Fig. 16(a). It can be noticed that the bus voltage is distorted and unbalanced, whereas the current waveforms of two inverters are not in the same shape, which indicates the presence of the circulating harmonic current between inverters. The waveforms are much improved with the proposed method shown in

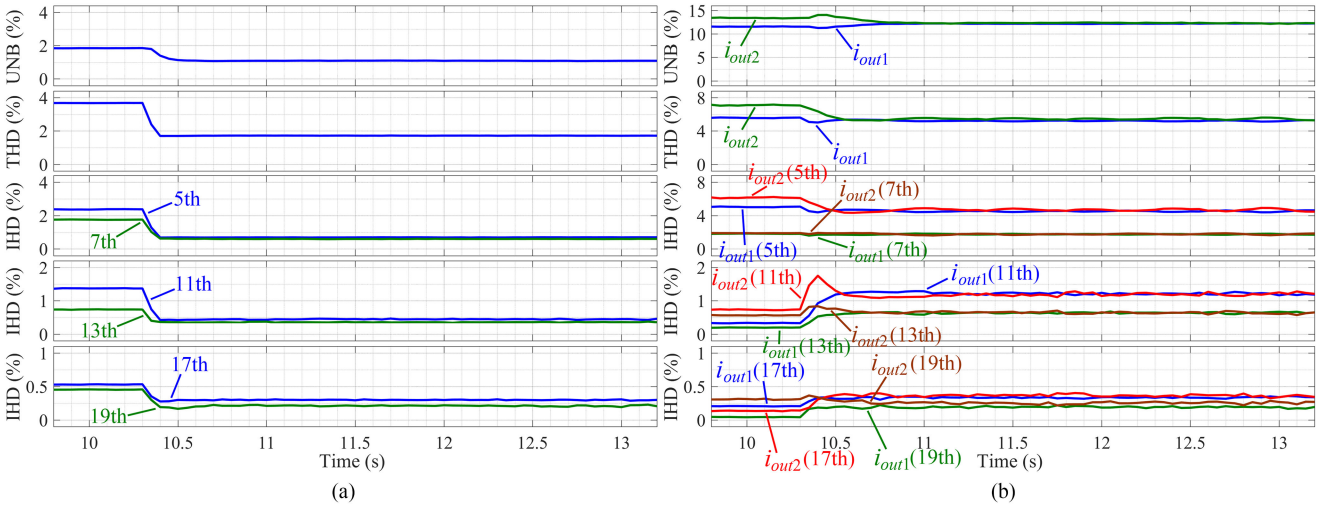

Fig. 17. UNB factors, THDs, and IHDs of (a) bus voltage and (b) inverter current when the proposed power quality compensation control is activated in Case 2.

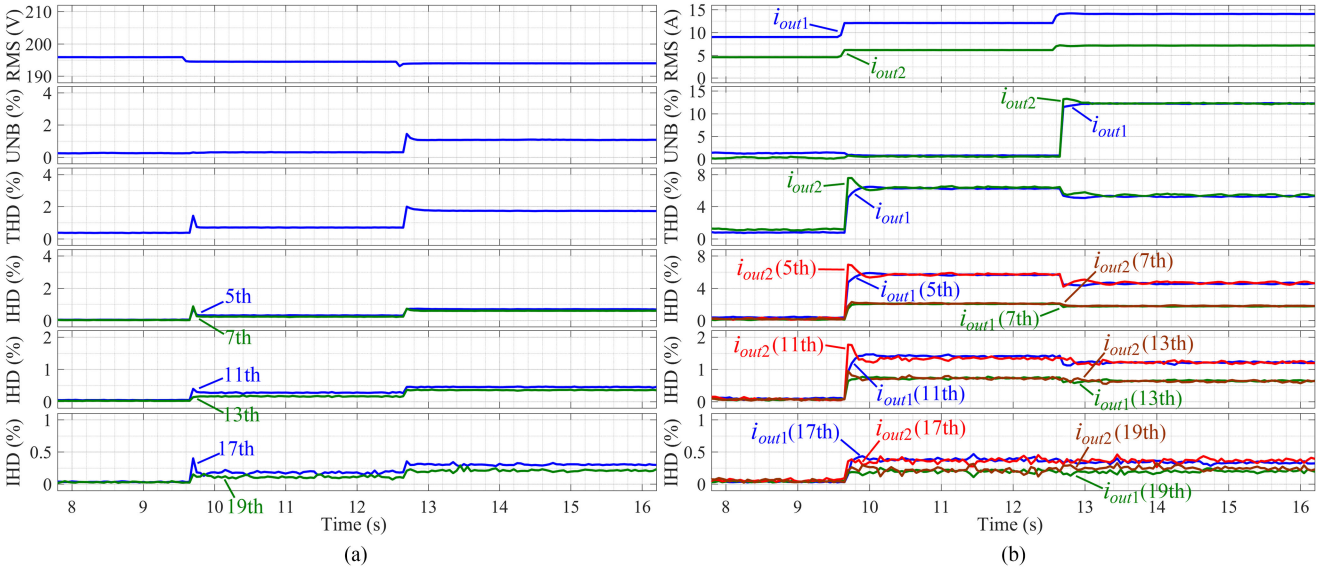

Fig. 18. UNB factors, THDs, and IHDs of (a) bus voltage and (b) inverter current during load transients in Case 3.

Fig. 16(b), in which the waveforms of the bus voltage become balanced and less distorted, and waveforms of the inverter current resemble each other. This suggests that the bus voltage is well compensated and the unbalanced/harmonic current is properly shared between inverters. It is noteworthy that if positive-virtual-impedance-based methods are applied, the bus voltage will become more distorted and unbalanced as bus voltage harmonic and negative sequences will increase due to the amplified harmonic and negative voltage drop on $|\boldsymbol{Z}^n_{\text{line}k} + \boldsymbol{Z}^n_{\text{inv}k}|$, as it is illustrated by Fig. 3.

The transient response of UNB factors, THDs, and IHDs of the bus voltage and inverter current is shown in Fig. 17. The proposed control is activated at around 10.3 s, and steady state is reached within 0.1 s for bus voltage distortions and within 0.3 s for inverter current distortions. UNB factors respond slightly slower, which are less than 0.2 s for the bus voltage and 0.5 s for the inverter current. At steady state, the UNB factor of the bus voltage is reduced from 1.85% to 1.09%, and THD is reduced from 3.68% to 1.72%. Meanwhile, UNB factors and harmonic distortions of the output current reached almost the same values, which indicate a well sharing of current sequences according to the power rating ratio of inverters. It is interesting that some

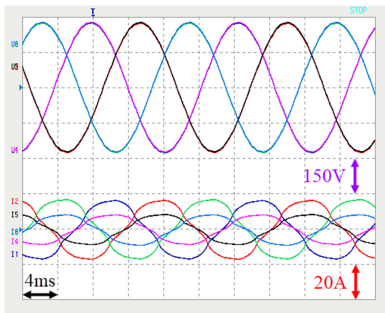

Fig. 19. Steady-state waveforms of the bus line voltage (upper) and the inverter current (lower) after the first transient in Case 3.

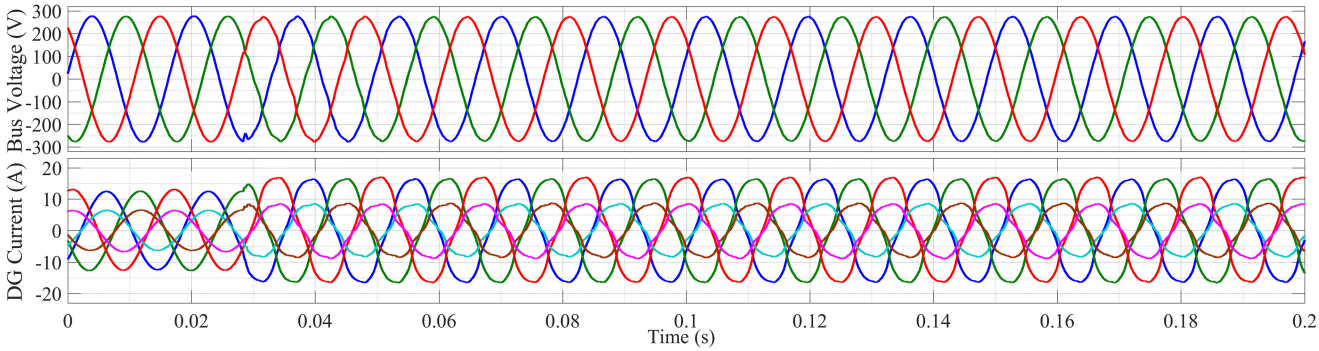

Fig. 20. Transient waveforms of bus line voltage (upper) and inverter current (lower) during the first transient in Case 3.

harmonic orders of the DG currents decrease, whereas the other harmonic orders increase. This is because the compensated bus voltage reshapes the total load current sequences.

Still, small distortions can be noticed in bus voltage waveforms of Fig. 16(b), which contribute to the 1.72% THD. The cause of residual bus voltage distortions will be further discussed in next part of this section.

C. Case 3: Load Transients

In Case 3, the proposed control is activated all the time, whereas its performance during load transients is shown in Fig. 18. Initially, only the 3P *RL* load is connected. The 3P rectifier load is connected at around 9.6 s, and the 2P *RL* load is connected around 12.6 s. It can be concluded that the transient response is very fast after each load transients, with settling times similar to those in Case 2. The RMS value of the bus voltage decreases after load connections due to the droop characteristics of the power generation control, which lead to proper sharing of inverter current RMS values. At steady state, UNB factors and harmonic distortions of the two inverter-interfaced DGs are always kept to be the same.

It can be noticed that harmonic distortions of the bus voltage increase after both load transients. For the first transient from the rectifier load, bus voltage THD increase from 0.37% to 0.69%, mainly because the increased load harmonic current sequences result in larger drooped voltage sequence errors, as it is illustrated in Fig. 10. For the second transient from the unbalanced load, bus voltage THD increases from 0.69% to 1.72% with notable increase in all measured IHD, whereas current harmonic distortions do not change significantly. This increased distortions, which can be further confirmed from the waveforms shown in Figs. 16(b) and 19, mainly result from uncontrolled harmonic sequences, such as $+5$th, -7th, $+11$th, -13th, $+17$th, and -19th, which are introduced by the load unbalance. If dedicated controllers for these sequences are added to the control frame, bus voltage distortions will be further reduced under the condition that both nonlinear load and unbalanced load are connected. However, as these sequences generally only appear in the unbalanced loading condition and are relatively small, dedicated controllers for them are not included in this paper.

Transient waveforms of the bus line voltage and inverter current during the first loading transient in Case 3 are shown in Fig. 20. It can be concluded that noticeable bus voltage distortions disappear after one or two cycles and proper current sharing is kept throughout the transient.

TABLE III
EXECUTION TIME OF THE PROPOSED CONTROL

Harmonic Sequences	1.25 GHz DSP (Measured)	150 MHz DSP (Estimated)
Up to 19th	9.44 µs	75.5 µs
Up to 13th	7.89 µs	63.1 µs
Up to 7th	6.30 µs	50.4 µs

D. Execution Time

Although power generation part and negative and six harmonic sequences are controlled, respectively, the control program of each inverter is executed within 9.44 μs, which is fast enough for the 18-kHz control frequency in this study. As the 1.25-GHz DSP used in this study is a high-performance one, estimated execution times in a typical 150-MHz DSP are listed in Table III according to the frequency ratio. From this table, it can be concluded that even with a 150-MHz DSP, the complete proposed control can be applied at a control frequency no higher than 13 kHz. If controllers for harmonic sequences higher than seventh are not included, 18-kHz control frequency is also realizable. Considering foreseeable further progress of the DSP, execution time is not an issue for the proposed control.

VIII. CONCLUSION

A cost-function-based decentralized power quality compensation method realizing, simultaneously, the bus voltage compensation and inverter current sharing is proposed in this paper. Unlike previous methods based on virtual impedance, the proposed method is not restrained by the tradeoff between the bus voltage quality and mitigation of inverter nonlinearities. Therefore, it becomes the first method, to the best of the authors' knowledge, to realize simultaneous bus voltage compensation and negative and harmonic current sequences sharing under the condition that inverter nonlinearities are not negligible. The plant modeling, including the consideration of nonlinearities of inverters, the unknown presence of other sources and unknown loading feature is discussed in detail, followed by the design of the observers and MPCs, which are the recommended tools to optimize the proposed cost functions. Tuning of the weighting

factors of MPCs is the key for the desirable balance between the bus voltage compensation and current sharing accuracy, and for the tradeoff between stability and transient dynamics. The complexity of the proposed inverter control is acceptable as it is demonstrated that its total execution time in a DSP can be limited within 9.44 μs. As it is verified by the experimental result, despite of the presence of considerable inverter nonlinearities, the proposed power quality compensation method achieves excellent transient and steady-state performance regarding simultaneous bus voltage compensation and inverter current sharing under any given loading condition, without any communication, upper level controller, or bus voltage measurement.

REFERENCES

[1] R. H. Lasseter, "MicroGrids," in *Proc. IEEE Power Eng. Soc. Winter Meeting*, 2002, pp. 305–308.

[2] M. M. Hashempour, M. Savaghebi, J. C. Vasquez, and J. M. Guerrero, "A control architecture to coordinate distributed generators and active power filters coexisting in a microgrid," *IEEE Trans. Smart Grid*, vol. 7, no. 5, pp. 2325–2336, Sep. 2016.

[3] J. He, Y. W. Li, D. Bosnjak, and B. Harris, "Investigation and active damping of multiple resonances in a parallel-inverter-based microgrid," *IEEE Trans. Power Electron.*, vol. 28, no. 1, pp. 234–246, Jan. 2013.

[4] D. H. Lee and J. W. Ahn, "A simple and direct dead-time effect compensation scheme in PWM-VSI," *IEEE Trans. Ind. Appl.*, vol. 50, no. 5, pp. 3017–3025, Sep./Oct. 2014.

[5] J. M. Guerrero, J. Matas, L. García de Vicuña, M. Castilla, and J. Miret, "Wireless-control strategy for parallel operation of distributed generation inverters," *IEEE Trans. Ind. Electron.*, vol. 53, no. 5, pp. 1461–1470, Oct. 2006.

[6] J. M. Guerrero, J. Matas, L. García de Vicuña, M. Castilla, and J. Miret, "Decentralized control for parallel operation of distributed generation inverters using resistive output impedance," *IEEE Trans. Ind. Electron.*, vol. 54, no. 2, pp. 994–1004, Apr. 2007.

[7] D. De and V. Ramanarayanan, "Decentralized parallel operation of inverters sharing unbalanced and nonlinear loads," *IEEE Trans. Power Electron.*, vol. 25, no. 12, pp. 3015–3025, Dec. 2010.

[8] T. Vandoorn, B. Meersman, J. D. Kooning, and L. Vandevelde, "Controllable harmonic current sharing in islanded microgrids: DG units with programmable resistive behavior toward harmonics," *IEEE Trans. Power Del.*, vol. 27, no. 2, pp. 831–841, Apr. 2012.

[9] X. Wang, F. Blaabjerg, and Z. Chen, "Autonomous control of inverter-interfaced distributed generation units for harmonic current filtering and resonance damping in an islanded microgrid," *IEEE Trans. Ind. Appl.*, vol. 50, no. 1, pp. 452–461, Jan./Feb. 2014.

[10] P. Sreekumar and V. Khadkikar, "A new virtual harmonic impedance scheme for harmonic power sharing in an islanded microgrid," *IEEE Trans. Power Del.*, vol. 31, no. 3, pp. 936–945, Jun. 2016.

[11] X. Chen, X. Ruan, D. Yang, W. Zhao, and L. Jia, "Injected grid current quality improvement for a voltage-controlled grid-connected inverter," *IEEE Trans. Power Electron.*, vol. 33, no. 2, pp. 1247–1258, Feb. 2018.

[12] P. Sreekumar and V. Khadkikar, "Direct control of the inverter impedance to achieve controllable harmonic sharing in the islanded microgrid," *IEEE Trans. Ind. Electron.*, vol. 64, no. 1, pp. 827–837, Jan. 2017.

[13] Q. C. Zhong, "Harmonic droop controller to reduce the voltage harmonics of inverters," *IEEE Trans. Ind. Electron.*, vol. 60, no. 3, pp. 936–945, Mar. 2013.

[14] T.-L. Lee and P.-T. Cheng, "Design of a new cooperative harmonic filtering strategy for distributed generation interface converters in an islanding network," *IEEE Trans. Power Electron.*, vol. 2, no. 5, pp. 1919–1927, Jul. 2007.

[15] J. He, Y. W. Li, J. M. Guerrero, F. Blaabjerg, and J. C.Vasquez, "An islanding microgrid power sharing approach using enhanced virtual impedance control scheme," *IEEE Trans. Power Electron.*, vol. 28, no. 11, pp. 5272–5282, Nov. 2013.

[16] J. He, Y. W. Li, and F. Blaabjerg, "An enhanced islanding microgrid reactive power, imbalance power, and harmonic power sharing scheme," *IEEE Trans. Power Electron.*, vol. 30, no. 6, pp. 3389–3401, Jun. 2015.

[17] Y. Han, P. Shen, X. Zhao, and J. M. Guerrero, "An enhanced power sharing scheme for voltage unbalance and harmonics compensation in an islanded ac microgrid," *IEEE Trans. Energy Convers.*, vol. 31, no. 3, pp. 1037–1050, Sep. 2016.

[18] J. He, B. Liang, Y. W. Li, and C. Wang, "Simultaneous microgrid voltage and current harmonics compensation using coordinated control of dual-interfacing converters," *IEEE Trans. Power Electron.*, vol. 32, no. 4, pp. 2647–2660, Apr. 2017.

[19] M. Hamzeh, S. Emamian, H. Karimi, and J. Mahseredjian, "Robust control of an islanded microgrid under unbalanced and nonlinear load conditions," *IEEE J. Emerg. Sel. Topics Power Electron.*, vol. 4, no. 2, pp. 512–520, Jun. 2016.

[20] M. S. Golsorkhi and D. D. C. Lu, "A decentralized control method for islanded microgrids under unbalanced conditions," *IEEE Trans. Power Del.*, vol. 31, no. 3, pp. 1112–1121, Jun. 2016.

[21] J. Liu, Y. Miura, and T. Ise, "Model-predictive-control-based distributed control scheme for bus voltage unbalance and harmonics compensation in microgrids," in *Proc. IEEE Energy Convers. Congr. Expo.*, Cincinnati, OH, USA, 2017, pp. 4439–4446.

[22] P. Cortes, M. P. Kazmierkowski, R. M. Kennel, D. E. Quevedo, and J. Rodriguez, "Predictive control in power electronics and drives," *IEEE Trans. Ind. Electron.*, vol. 55, no. 12, pp. 4312–4324, Dec. 2008.

[23] S. Bolognani, S. Bolognani, L. Peretti, and M. Zigliotto, "Design and implementation of model predictive control for electrical motor drives," *IEEE Trans. Ind. Electron.*, vol. 56, no. 6, pp. 1925–1936, Jun. 2009.

[24] Y. Wang, Z. Chen, X. Wang, Y. Tian, Y. Tan, and C. Yang, "An estimator-based distributed voltage-predictive control strategy for ac islanded microgrids," *IEEE Trans. Power Electron.*, vol. 30, no. 7, pp. 3934–3951, Jul. 2015.

[25] Y. Wang, X. Wang, Z. Chen, and F. Blaabjerg, "Distributed optimal control of reactive power and voltage in islanded microgrids," *IEEE Trans. Ind. Appl.*, vol. 53, no. 1, pp. 340–349, Jan./Feb. 2017.

[26] A. A. Ahmed, B. K. Koh, and Y. I. Lee, "A comparison of finite control set and continuous control set model predictive control schemes for speed control of induction motors," *IEEE Trans. Ind. Informat.*, vol. 14, no. 4, pp. 1334–1346, Apr. 2018.

[27] T. Dragicevic, M. Alhasheem, M. Lu, and F. Blaabjerg, "Improved model predictive control for high voltage quality in microgrid applications," in *Proc. IEEE Energy Convers. Congr. Expo.*, Cincinnati, OH, USA, 2017, pp. 4475–4480.

[28] Q.-C. Zhong, P.-L. Nguyen, Z. Ma, and W. Sheng, "Self-synchronized synchronverters: Inverters without a dedicated synchronization unit," *IEEE Trans. Power Electron.*, vol. 29, no. 2, pp. 617–630, Feb. 2014.

[29] J. Liu, Y. Miura, H. Bevrani, and T. Ise, "Enhanced virtual synchronous generator control for parallel inverters in microgrids," *IEEE Trans. Smart Grid*, vol. 8, no. 5, pp. 2268–2277, Sep. 2017.

[30] J. Liu, Y. Miura, and T. Ise, "A novel oscillation damping method of virtual synchronous generator control without PLL using pole placement," in *Proc. Int. Power Electron. Conf.*, Niigata, Japan, 2018, pp. 775–781.

[31] J. Liu, Y. Miura, and T. Ise, "Comparison of dynamic characteristics between virtual synchronous generator and droop control in inverter-based distributed generators," *IEEE Trans. Power Electron.*, vol. 31, no. 5, pp. 3600–3611, May 2016.

[32] S. D'Arco, J. A. Suul, and O. B. Fosso, "Automatic tuning of cascaded controllers for power converters using eigenvalue parametric sensitivities," *IEEE Trans. Ind. Appl.*, vol. 51, no. 2, pp. 1743–1753, Mar./Apr. 2015.

[33] M. C. Chandorkar, D. M. Divan, and R. Adapa, "Control of parallel connected inverters in standalone ac supply systems," *IEEE Trans. Ind. Appl.*, vol. 29, no. 1, pp. 136–143, Jan./Feb. 1993.

[34] J. M. Guerrero, L. García de Vicuña, J. Matas, M. Castilla, and J. Miret, "A wireless controller to enhance dynamic performance of parallel inverters in distributed generation systems," *IEEE Trans. Power Electron.*, vol. 9, no. 5, pp. 1205–1213, Sep. 2004.

[35] L. Asiminoael, F. Blaabjerg, and S. Hansen, "Detection is key—Harmonic detection methods for active power filter applications," *IEEE Ind. Appl. Mag.*, vol. 13, no. 4, pp. 22–33, Jul./Aug. 2007.

[36] E. W. Kamen and J. K. Su, *Introduction to Optimal Estimation*. London, U.K.: Springer-Verlag, 1999, pp. 163–171.

[37] J. M. Maciejowski, *Predictive Control: With Constraints*. Englewood Cliffs, NJ, USA: Prentice Hall, 2002, pp. 74–81.

Jia Liu (S'15–M'17) received the B.E. and M.E. degrees from the Xi'an Jiaotong University, Xi'an, China, in 2008 and 2011, respectively, the Diplôme d'Ingénieur degree from the University of Technology of Troyes, Troyes, France, in 2011, and the Ph.D. degree in engineering from Osaka University, Osaka, Japan, in 2016.

He was with Delta Electronics (Jiangsu), Ltd., Nanjing, China, from 2011 to 2012. Since 2016, he has been with the Division of Electrical, Electronic and Information Engineering, Graduate School of Engineering, Osaka University, where he is currently an Assistant Professor. His research interests include distributed generators, microgrids, power quality, and motor drives.

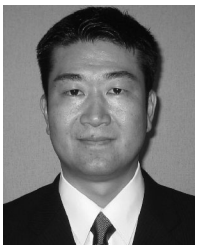

Yushi Miura (M'06) received the doctoral degree in electrical and electronic engineering from the Tokyo Institute of Technology, Tokyo, Japan, in 1995.

From 1995 to 2004, he was with the Japan Atomic Energy Research Institute as a Researcher and developed power supplies and superconducting coils for nuclear fusion reactors. Since 2004, he has been an Associate Professor with the Division of Electrical, Electronic and Information Engineering, Osaka University, Osaka, Japan. His research interests include applications of power electronics for power systems.

Toshifumi Ise (M'86) received the B.E., M.E., and doctor of engineering degrees in electrical engineering from Osaka University, Osaka, Japan, in 1980, 1982 and 1986, respectively.

He is a Professor Emeritus with Osaka University and the President of NARA-GAKUEN Incorporated Educational Institution. From 1986 to 1990, he was with the Nara National College of Technology, Nara, Japan. Since 1990, he has been with the Faculty of Engineering and Graduate School of Engineering, Osaka University, where he was a Professor from August 2002 to March, 2018. His research interests include the areas of power electronics and applied superconductivity for power systems.

Prof. Ise is a fellow of the Institute of Electrical Engineers of Japan.